Article

SOURCE DATA | TRANSPARENT PROCESS | OPEN ACCESS

THE EMBO JOURNAL

Single-molecule imaging reveals Tau trapping at nanometer-sized dynamic hot spots near the plasma membrane that persists after microtubule perturbation and cholesterol depletion

Pranesh Padmanabhan[1,*], Andrew Kneynsberg[1], Esteban Cruz[1], Rumelo Amor[2], Jean-Baptiste Sibarita[3] & Jürgen Götz[1,**]

Abstract

Accumulation of aggregates of the microtubule-binding protein Tau is a pathological hallmark of Alzheimer's disease. While Tau is thought to primarily associate with microtubules, it also interacts with and localizes to the plasma membrane. However, little is known about how Tau behaves and organizes at the plasma membrane of live cells. Using quantitative, single-molecule imaging, we show that Tau exhibits spatial and kinetic heterogeneity near the plasma membrane of live cells, resulting in the formation of nanometer-sized hot spots. The hot spots lasted tens of seconds, much longer than the short dwell time (~ 40 ms) of Tau on microtubules. Pharmacological and biochemical disruption of Tau/microtubule interactions did not prevent hot spot formation, suggesting that these are different from the reported Tau condensation on microtubules. Although cholesterol removal has been shown to reduce Tau pathology, its acute depletion did not affect Tau hot spot dynamics. Our study identifies an intrinsic dynamic property of Tau near the plasma membrane that may facilitate the formation of assembly sites for Tau to assume its physiological and pathological functions.

Keywords Alzheimer's disease; nanodomains; single-molecule imaging; super-resolution microscopy; Tau
Subject Categories Neuroscience; Membrane & Trafficking
DOI 10.15252/embj.2022111265 | Received 24 March 2022 | Revised 20 July 2022 | Accepted 22 July 2022 | Published online 25 August 2022
The EMBO Journal (2022) 41: e111265

Introduction

Tau is conventionally thought of as a protein that primarily associates with microtubules, thereby regulating their stability (Polanco *et al*, 2018; Brandt *et al*, 2020; Chang *et al*, 2021). However, as an intrinsically disordered protein, Tau has remarkable structural flexibility and also undergoes various post-translational modifications, allowing it to interact with numerous binding partners and execute multiple cellular functions (Polanco *et al*, 2018, Brandt *et al*, 2020, Chang *et al*, 2021), including axonal transport (Vershinin *et al*, 2007; Dixit *et al*, 2008; Kanaan *et al*, 2011), neuronal maturation (Caceres & Kosik, 1990; Knops *et al*, 1991), and protein translation (Evans *et al*, 2019, 2021). Interest in the behavior of Tau at the plasma membrane was spurred firstly by the realization that, in an Alzheimer's disease context, toxic Tau aggregates cross the plasma membrane for release into the extracellular milieu, thereby contributing to the spread of Tau across interconnected brain regions, a process believed to underlie the pathology in Alzheimer's disease and other tauopathies (Braak & Del Tredici, 2011; Polanco *et al*, 2018, 2021). Secondly, in an ill-defined physiological context, Tau lacking a classical signal peptide undergoes unconventional secretion (Katsinelos *et al*, 2018; Merezhko *et al*, 2018).

The association of Tau with the plasma membrane can occur directly through electrostatic interactions with anionic lipids (Georgieva *et al*, 2014; Mari *et al*, 2018) and indirectly through interactions with membrane-associated proteins, such as the Src kinase Fyn (Pooler *et al*, 2012), the motor protein dynactin (Magnani *et al*, 2007), and the phospholipid-binding protein annexin A2 (Gauthier-Kemper *et al*, 2011). Moreover, Tau interacts with microtubules and actin filaments, anchoring them to the plasma membrane (Sallaberry *et al*, 2021), but whether Tau forms aggregates near the plasma membrane is unknown. So far, studies using artificial lipid membranes have suggested that membrane binding can cause conformational changes to Tau (Majewski *et al*, 2020), initiate Tau aggregation and fibrilization (Elbaum-Garfinkle *et al*, 2010; Fanni *et al*, 2019), and mediate Tau-induced membrane permeabilization and toxicity (Flach *et al*, 2012; Patel *et al*, 2015). However, despite the critical importance of Tau-membrane interactions (Brandt *et al*,

1 Clem Jones Centre for Ageing Dementia Research, Queensland Brain Institute, The University of Queensland, Brisbane, QLD, Australia
2 Queensland Brain Institute, The University of Queensland, Brisbane, QLD, Australia
3 Université de Bordeaux, Interdisciplinary Institute for Neuroscience, UMR, Bordeaux, France
*Corresponding author. Tel: +61 7 3346 6300; E-mail: p.padmanabhan@uq.edu.au
**Corresponding author. Tel: +61 7 3346 6329; E-mail: j.goetz@uq.edu.au

1995; Arrasate *et al*, 2000; Pooler *et al*, 2012; Katsinelos *et al*, 2018; Merezhko *et al*, 2018), quantifying how Tau behaves and organizes at the plasma membrane in a live cellular environment has proven challenging due to the lack of sensitive tools, thereby limiting our understanding of how this protein executes its physiological and pathological functions in this compartment (Padmanabhan *et al*, 2021).

Here, using single-molecule-based super-resolution microscopy, we investigated both the dynamics and nanoscale organization of Tau near the plasma membrane of live cells. We found that Tau exhibited immobile, confined, and free diffusive states and formed nanometer-sized hot spots. Moreover, the confinement and immobilization of Tau were due to its trapping on microtubules and in the hot spots. We found that, although inhibiting Tau/microtubule interactions released Tau from microtubules and increased its mobility, the heterogeneous mobility pattern persisted, and surprisingly, the dynamics of the Tau hot spots was unaltered. Moreover, these hot spots persisted after the depletion of cholesterol, which is known to reduce Tau pathology in transgenic mice (Boimel *et al*, 2009). Here, we suggest a model whereby the dynamic partitioning of Tau into different kinetic pools equips Tau with the dynamic properties to form assemblies near the plasma membrane as a critical step in pathological dysregulation.

Results

Single-molecule tracking of tau near the plasma membrane

To visualize and track individual Tau molecules near the inner leaflet of the plasma membrane, we transiently expressed the most prevalent human isoform of Tau (0N4R, 383 amino acids) fused carboxy-terminally to photoactivatable fluorescent protein mEos3.2 (hereafter abbreviated to Tau^{WT}-mEos3.2) in murine N2a neuroblastoma cells (Fig 1A; Appendix Fig S1). We then used total internal reflection fluorescence (TIRF) illumination (Fig 1B) to perform single-particle tracking photoactivated localization microscopy (sptPALM) (Manley *et al*, 2008) at 50 Hz for a duration of 160 s. This allowed visualization of the substrate-attached cell surface comprising the plasma membrane and its subjacent cytoskeleton with ~ 100 nm axial resolution (Fig 1C). This imaging paradigm has provided critical insights into the interactions of intracellular signaling molecules, such as Rac1 (Mehidi *et al*, 2019) and KRas (Lee *et al*, 2019), and scaffolding proteins, including caveolins (Gormal *et al*, 2020), with the plasma membrane. Capitalizing on this approach, we first captured a diffraction-limited TIRF image of Tau^{WT}-mEos3.2 before photoconversion in the green (491 nm) emission channel (Fig 1D). We then recorded a time series of detections of photoconverted Tau^{WT}-mEos3.2 molecules near the plasma membrane in the red (561 nm) emission channel, with a localization precision of $\sim 45 \pm 6.9$ nm (mean ± s.d.) (Fig 1E and F; Appendix Fig S2). This allowed us to construct $4{,}764 \pm 2{,}504$ and 749 ± 506 (mean ± s.d.) Tau^{WT}-mEos3.2 trajectories per cell that lasted at least 8 and 20 consecutive image frames, respectively (Fig 1E; Appendix Fig S3). Given that free cytosolic molecules have a large diffusion coefficient of ~ 10–100 $\mu m^2/s$ (Kühn *et al*, 2011; Gura Sadovsky *et al*, 2017), they would not last ≥8 consecutive frames under TIRF illumination (Rossier *et al*, 2012). Thus, the detected trajectories likely represent Tau molecules interacting with the plasma membrane components and the associated cytoskeleton. In line with this notion, only a few free cytosolic mEos3.2 trajectories were detected in the TIRF plane with our imaging conditions (Appendix Fig S3).

Tau exhibits a heterogeneous mobility pattern near the plasma membrane

We investigated the mobility pattern of Tau by analyzing its trajectories. Typically, the interaction of a protein with itself or different plasma membrane-associated components manifests as different motion states, ranging from almost stationary to freely diffusive and directed movements (Jacobson *et al*, 2019). We therefore investigated whether Tau is static or dynamic near the plasma membrane by comparing the mobility of Tau molecules in live and fixed cells. For this, we computed the average mean square displacement (MSD) and the frequency distribution of the instantaneous diffusion coefficient of all trajectories from each analyzed cell (Fig 1G–J). As expected, the slope of the average MSD curve increased, and the diffusion coefficient distribution was broader and shifted towards higher values in live cells compared with fixed cells, indicating the presence of mobile and immobile pools of Tau molecules near the plasma membrane in the live cells (Fig 1G–J; Appendix Fig S4).

Figure 1. Tau displays heterogeneous mobility patterns near the plasma membrane.

A Schematic of the most prevalent 0N4R Tau isoform carboxy-terminally tagged with mEos3.2 (Tau^{WT}-mEos3.2).
B Schematic of the detection of Tau^{WT}-mEos3.2 molecules in a TIRF microscopy setup.
C Schematic of the plasma membrane and subjacent cytoskeleton captured using TIRF imaging as shown in panel (B).
D Representative diffraction-limited TIRF image of an N2a cell expressing Tau^{WT}-mEos3.2 acquired in the green emission channel before sptPALM imaging.
E, F Maps of trajectories (E) and intensities (F) of Tau^{WT}-mEos3.2 molecules corresponding to the boxed region highlighted in (D). The color bar in (F) indicates the local density of each detection computed within a radius of 30 nm.
G–J Comparison of Tau^{WT}-mEos3.2 mobility parameters in live and fixed cells. (G) Average MSD as a function of time and (H) the corresponding area under the curve. (I) The distribution of the diffusion coefficients in a semi-log plot and (J) the corresponding mobile fraction.
K A map of trajectories annotated as immobile, confined, and free state using MSS analysis.
L A map of trajectories annotated as distinct diffusive states using the 3-state hidden Markov model.
M, N Fits (M) of 1-state (red dashed line), 2-state (magenta dashed line), and 3-state (green dashed line) models to the experimental data (black dotted line) and the root mean square error of all the tested models (N).

Data information: Error bars, s.e.m. $n = 14$ live cells and 14 fixed cells from $N = 2$ independent experiments. Statistical analysis was performed using the Mann–Whitney *U* test (H, J) and one-way ANOVA with the Dunnett multiple comparison correction (N).
Source data are available online for this figure.

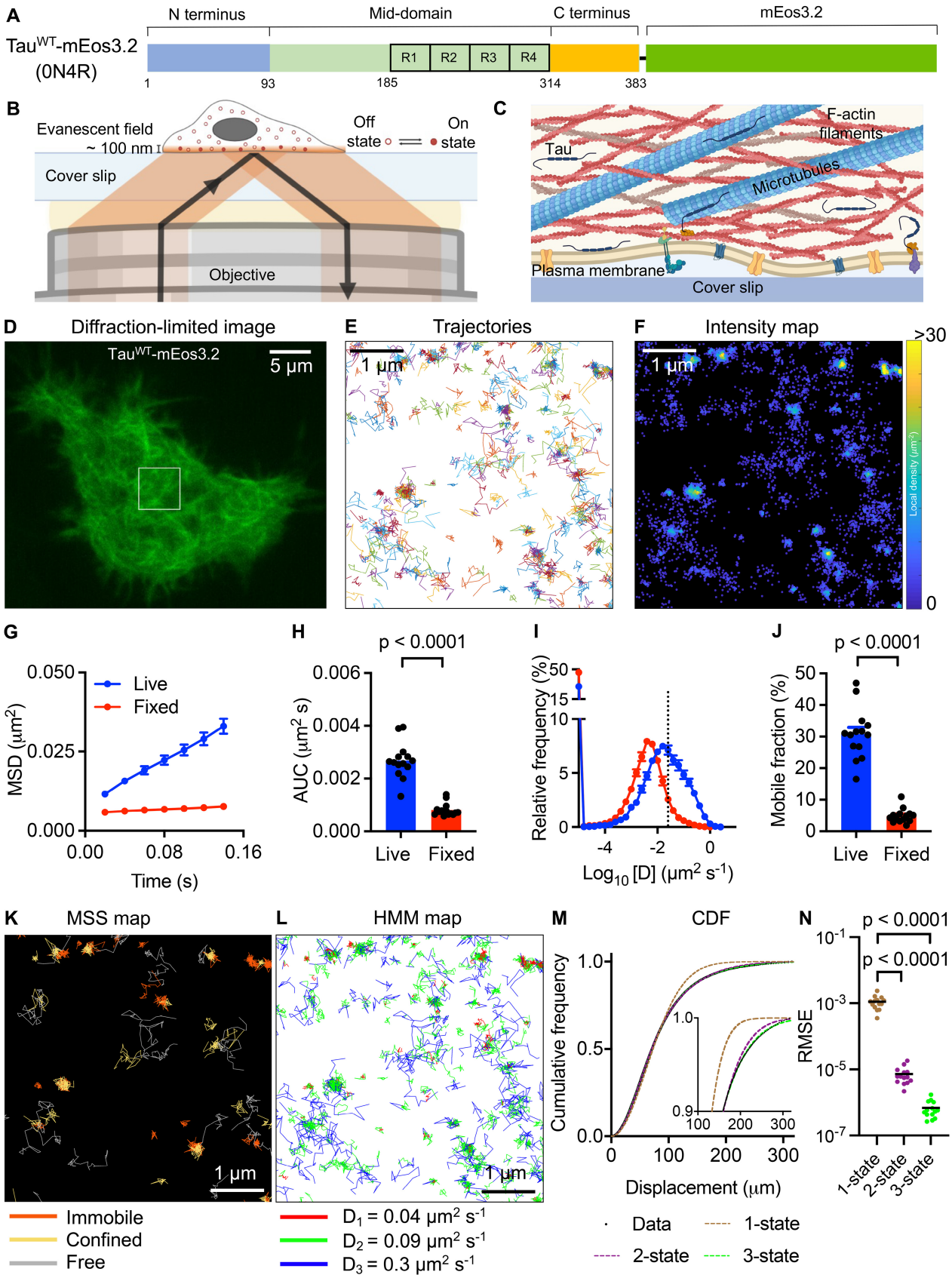
A
N terminus
Mid-domain
C terminus
mEos3.2
Tau^WT-mEos3.2
(0N4R)
R1
R2
R3
R4
1
93
185
314
383
B
Evanescent field
~ 100 nm
Off state
On state
Cover slip
Objective
C
F-actin filaments
Tau
Microtubules
Plasma membrane
Cover slip
D
Diffraction-limited image
Tau^WT-mEos3.2
5 µm
E
Trajectories
1 µm
F
Intensity map
1 µm
>30
Local density (µm⁻²)
0
G
MSD (µm²)
Live
Fixed
0.050
0.025
0.000
0.00
0.08
0.16
Time (s)
H
p < 0.0001
AUC (µm² s)
0.006
0.004
0.002
0.000
Live
Fixed
I
Relative frequency (%)
50
15
10
5
0
-4
-2
0
Log10 [D] (µm² s⁻¹)
J
p < 0.0001
Mobile fraction (%)
50
40
30
20
10
0
Live
Fixed
K
MSS map
1 µm
Immobile
Confined
Free
L
HMM map
1 µm
D1 = 0.04 µm² s⁻¹
D2 = 0.09 µm² s⁻¹
D3 = 0.3 µm² s⁻¹
M
CDF
Cumulative frequency
1.0
0.5
0.0
0
100
200
300
Displacement (µm)
1.0
0.9
100
200
300
Data
1-state
2-state
3-state
N
p < 0.0001
p < 0.0001
RMSE
10⁻¹
10⁻³
10⁻⁵
10⁻⁷
1-state
2-state
3-state

Figure 1.

We next performed a more detailed quantification of the complex motion pattern of Tau using several complementary approaches (Fig 1K–N). First, we performed moment scaling spectrum (MSS) analysis, a method that has been widely used to characterize motion states of receptors and transmembrane proteins (Jaqaman *et al*, 2011), and estimated the slope of the MSS of Tau^{WT}-mEos3.2 trajectories. We found that Tau existed in three motion states near the plasma membrane: immobile, confined, and freely diffusive (Fig 1K). The confinement radii of the immobile and confined states were 67.4 ± 20.7 nm and 89 ± 37.8 nm (mean ± s.d.), respectively (Appendix Fig S5A–C). We then analyzed the trajectories using hidden Markov models (HMMs), which assume that molecules are switching between discrete diffusive states to estimate the associated model parameters. This analysis revealed that Tau^{WT}-mEos3.2 molecules displayed at least three distinct diffusive states, with apparent diffusion coefficients of 0.04 ± 0.02, 0.11 ± 0.04 and 0.29 ± 0.02 μm^2/s (mean ± s.d.), ranging from immobile to confined to free diffusion (Materials and Methods; Fig 1L; Appendix Fig S5D–F). Finally, we fitted Brownian motion models to the cumulative frequency distribution of the frame-to-frame displacement of Tau^{WT}-mEos3.2 molecules and found that models with more than one diffusive state described the data well (Fig 1M and N). Together, these results provide evidence that Tau exhibits complex diffusion patterns near the plasma membrane, possibly reflecting its interactions with other Tau molecules or its partners in this compartment.

Tau forms dynamic nanometer-sized hot spots near the plasma membrane

Single-molecule imaging studies have revealed that receptors and signaling molecules form hot spots (a subset of which is known as nanoclusters or nanodomains) at the plasma membrane (Padmanabhan *et al*, 2021). We therefore examined whether the observed confined diffusion was due to the similar trapping of Tau in hot spots. Indeed, we found signatures of Tau hot spots with high localization density in the intensity maps that were not detectable in the diffraction-limited TIRF image (Fig 2A and B). We quantitatively characterized these regions based on both spatial and temporal correlations between individual detections associated with the hot spots as follows. Tessellation-based spatial segmentation algorithms have been widely used to quantify protein clusters from the sptPALM data (Levet *et al*, 2015; Padmanabhan *et al*, 2019). Using this approach, we first generated a Voronoï diagram of all localizations, with polygons centered on each single-molecule localization in cells (Fig 2C). We then identified the cell contour and the potential locations of Tau hot spots based on the normalized localization detection parameters (Materials and Methods; Fig 2D). Next, to characterize their temporal dynamics, we performed time-correlated PALM (tcPALM) analysis, which has previously revealed transient clustering of RNA polymerase (Cisse *et al*, 2013; Cho *et al*, 2018) and membrane receptors (Gormal *et al*, 2020). Here, we computed the time series of molecular detections of individual hot spots and found that the detections were not uniformly distributed but were correlated and clustered in time, indicating the transient nature of these hot spots near the plasma membrane (Fig 2E). This effect was more apparent in the cumulative detections of molecules, where we observed sudden changes in the slope of detection frequency, marking the duration during which we could detect the hot spots (Fig 2E). We also found that the trajectories within the hot spots were highly confined within a radius of 73.1 ± 30.9 nm (mean ± s.d.) (Fig 2F; Appendix Fig S5G). Furthermore, the mobility of Tau^{WT}-mEos3.2 molecules in the hot spots was significantly lower than their overall mobility (Fig 2G–I). To better characterize this confinement, we computed the angles between two successive translocations from three consecutive points and the angular distribution of Tau molecules within the hot spots (Fig 2J), which together help to elucidate the geometry of the local environment of the molecule (Izeddin *et al*, 2014). The angular distribution of Tau within the hot spots was shifted towards 180°, and this is significantly different from what would be expected from random motion (Fig 2J) but is consistent with motion within a confined space. We next estimated the apparent lifetime of each burst (burst duration) and the number of detections per burst (burst size). The average burst duration and size of the Tau hot spots were 11.7 ± 10.6 s and 136.3 ± 127.2 detection counts (mean ± s.d.), respectively (Fig 2K and L). Finally, we found that Tau^{WT}-mEos3.2 molecules also formed hot spots and displayed heterogeneous mobility patterns in HEK293T cells (Appendix Fig S6) similar to those observed in N2a cells, indicating that the dynamic behavior of Tau is conserved across cell types.

Tau hot spots are not static

To ascertain that the Tau hot spots were not an artifact due to the presence of the mEos3.2 tag, we performed single-molecule imaging of Tau^{WT} fused with the HaloTag (Tau^{WT}-HaloTag) in N2a cells incubated with a HaloTag ligand (Janelia Fluor 646). At a 100 pM

Figure 2. Tau hot spots form transiently near the plasma membrane.

A Representative diffraction-limited TIRF image of an N2a cell expressing Tau^{WT}-mEos3.2 acquired in the green channel before sptPALM imaging.
B–D Intensity map (B), Voronoï diagram (C), and hot spot map (D) of Tau^{WT}-mEos3.2 molecules corresponding to the boxed region highlighted in (A).
E Representative time series of detections from two Tau^{WT}-mEos3.2 hot spots highlighted in (D).
F Example trajectories detected within hot spots.
G Trajectories associated with hot spots are highlighted in blue and the remainder in cyan.
H, I Comparison of mobility parameters of Tau^{WT}-mEos3.2 molecules associated with hot spots and all the trajectories. Error bars, s.e.m.
J Angular distribution of the angle (θ) between the vectors of two successive translocation steps of molecules within hot spots (light blue) compared to that of simulated molecules undergoing Brownian motion (light red). θ is the angle between the vector joining the 1st and 2nd position and the vector connecting the 2nd and 3rd position.
K, L The distributions of burst duration (K) and size (L) of hot spots. The mean ± s.d. is shown together with the number of hot spots analyzed in brackets.

Data information: In (A–L), The analysis corresponds to experiments in Fig 1 (n = 14 cells from N = 2 independent experiments).
Source data are available online for this figure.

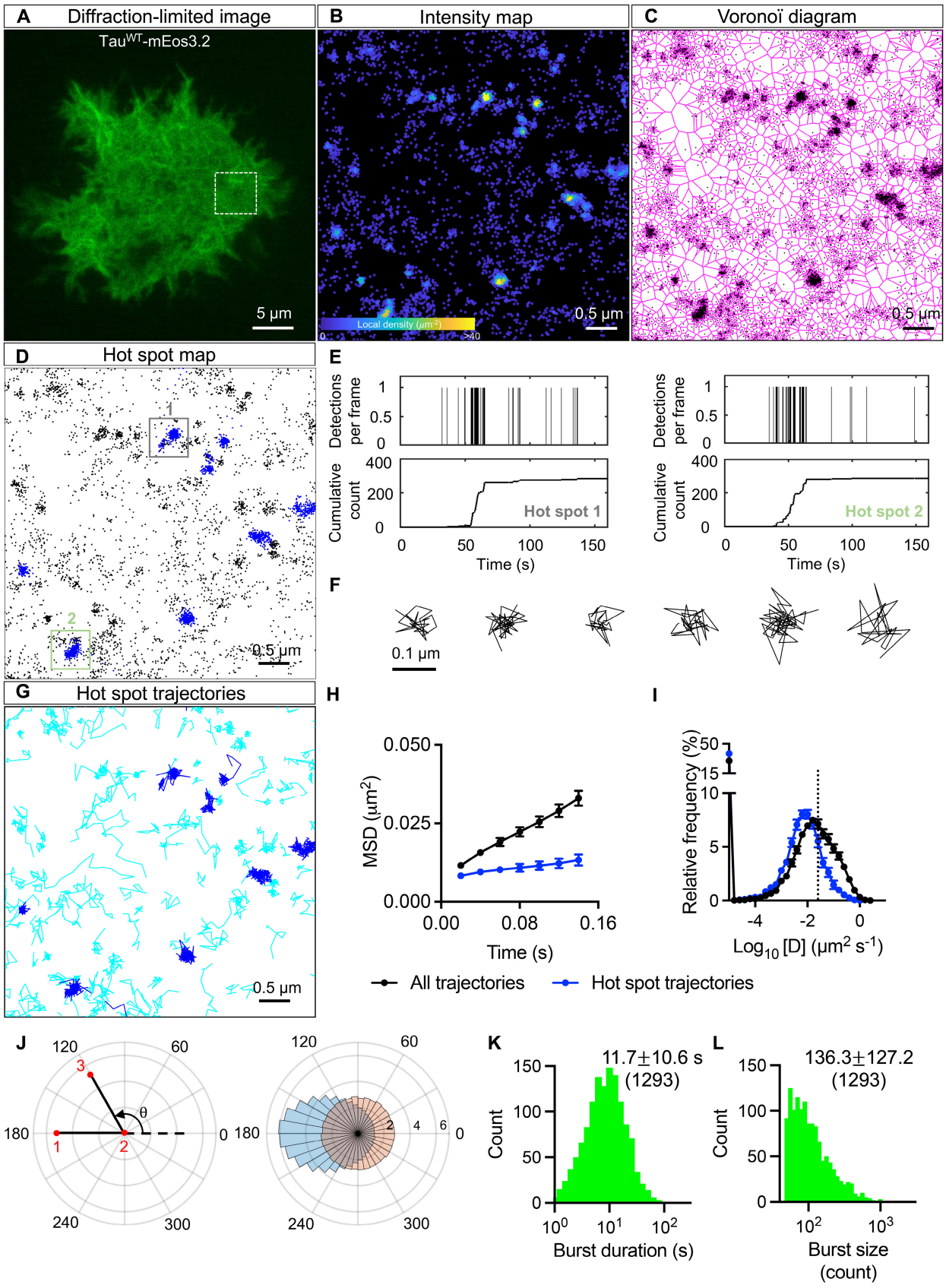
A Diffraction-limited image
Tau^WT-mEos3.2
5 µm
B Intensity map
Local density (µm⁻²)
0
>40
0.5 µm
C Voronoï diagram
0.5 µm
D Hot spot map
1
2
0.5 µm
E
Detections per frame
Cumulative count
Hot spot 1
Hot spot 2
Time (s)
F
0.1 µm
G Hot spot trajectories
0.5 µm
H
MSD (µm²)
Time (s)
I
Relative frequency (%)
Log10 [D] (µm² s⁻¹)
All trajectories
Hot spot trajectories
J
K
11.7±10.6 s
(1293)
Count
Burst duration (s)
L
136.3±127.2
(1293)
Count
Burst size
(count)

Figure 2.

concentration of the Halo ligand, we only obtained single-molecule signals in N2a cells transfected with Tau^{WT}-HaloTag but not in cells transfected with either the free HaloTag or Tau^{WT}-FLAG-Tag (Appendix Fig S7). By combining Voronoï tessellation-based spatial segmentation and tcPALM analyses, we observed that Tau^{WT}-HaloTag molecules also formed hot spots near the plasma membrane (Fig 3A–E). The average burst duration and size of these hot spots were 9.9 ± 13.5 s and 280.1 ± 496.9 detection counts (mean ± s.d.), respectively (Fig 3F–H). Membrane protein clusters often exhibit lateral mobility with functional consequences (Garcia-Parajo *et al*, 2014). For example, the mobility of DC-SIGN and LAT clusters are linked to virus internalization and T-cell signaling, respectively (Garcia-Parajo *et al*, 2014). We therefore wondered whether Tau hot spots also display movement. To test this, we constructed trajectories of Tau^{WT}-HaloTag hot spots at 0.2 s intervals over their lifetime (Fig 3I). We then quantified the MSD curves of hot spot trajectories and found that some hot spots were stationary whereas others were mobile (Fig 3J). Overall, these results demonstrate that Tau forms hot spots, which are dynamic near the cell surface.

Nocodazole-mediated microtubule disruption increases the mobility of individual tau molecules near the plasma membrane

Given that microtubules are a major binding partner of Tau and that they localize to and interact with the plasma membrane, we next asked whether the mobility pattern of Tau is affected by the availability of microtubules. Indeed, a diffraction-limited TIRF image of the Tau^{WT}-mEos3.2-expressing cells readily revealed microtubule-like structures indicative of the association of Tau with microtubules (Fig 4A). To assess the effect that microtubules have on the mobility of Tau, we treated N2a cells with either 5 μM of the microtubule-destabilizing agent nocodazole or DMSO (control) for up to 4 h. As expected, in the diffraction-limited TIRF images, the density of microtubule filament-like structures visualized by Tau^{WT}-mEos3.2 molecules was markedly reduced in the nocodazole-treated compared with DMSO-treated live cells (Fig 4A and B; Appendix Fig S8A). A similar effect was observed when imaging the same cell before and after nocodazole treatment (Appendix Fig S8B). We also saw a similar decrease in microtubule filaments in fixed, nocodazole-treated N2a cells stained with an anti-tubulin antibody (Appendix Fig S9). However, consistent with what has been previously reported (Xu *et al*, 2017), we did observe a few nocodazole-resistant microtubules. Remarkably, the trajectory maps showed that Tau molecules could be detected in both DMSO- and nocodazole-treated cells (Fig 4C and D). We also found that the mobility of Tau was greater in the nocodazole-treated compared with the control cells, as assessed by changes in the average MSD curve (Fig 4E), the area under the MSD curve (Fig 4F), the frequency distribution of diffusion coefficients (Fig 4G), and the percentage of the mobile fraction (Fig 4H).

Microtubule-binding-deficient mutant tau molecules has increased mobility near the plasma membrane

To further validate our findings, we generated a pseudophosphorylated mutant Tau tagged with mEos3.2 by introducing two serine to glutamate mutations at positions 262 and 356 in the microtubule-binding domain ($Tau^{S262E/S356E}$-mEos3.2) that reduce Tau's binding affinity to microtubules (Chen *et al*, 2006) (Fig 5A). As expected, the microtubule filament-like structures were barely visible in $Tau^{S262E/S356E}$-mEos3.2-expressing cells compared to those expressing Tau^{WT}-mEos3.2 (Fig 5B and C; Appendix Fig S10), indicating a reduced association of the mutant Tau with microtubules. Nonetheless, we could readily detect and track a similar number of molecules in both Tau^{WT}-mEos3.2- and $Tau^{S262E/S356E}$-mEos3.2-expressing cells (Fig 5D and E; Appendix Fig S11A). Consistent with our nocodazole experiments, we found that $Tau^{S262E/S356E}$-mEos3.2 had higher mobility than Tau^{WT}-mEos3.2 molecules (Fig 5F–I). For both microtubule perturbation conditions, HMM analysis revealed that Tau molecules displayed distinct diffusive states (Appendix Fig S11). Together, these results indicate that the mobility of Tau increases when it is released from microtubules and that the protein exhibits heterogeneous mobility patterns even when Tau/microtubule interactions are prevented.

Tau hot spots are resistant to microtubule perturbations and cholesterol depletion

Finally, we investigated the effect of microtubule perturbations on the dynamics of the Tau hot spots. We were able to detect transient hot spots of Tau^{WT}-mEos3.2 in nocodazole-treated cells (Fig 6A–G) and of $Tau^{S262E/S356E}$-mEos3.2 in untreated cells (Fig 6H–N). In nocodazole-treated cells, the burst duration, burst size, and density of Tau^{WT}-mEos3.2 hot spots were 14.9 ± 17.5 s, 174.4 ± 266.3 detection counts, and 0.45 ± 0.16 spots/μm^2 (mean ± s.d.). In untreated cells expressing $Tau^{S262E/S356E}$-mEos3.2, the burst duration, burst size, and density of Tau^{WT}-mEos3.2 hot spots were 13.1 ± 13.1 s, 161.2 ± 189.2 detection counts, and 0.39 ± 0.17 spots/μm^2 (mean ± s.d.). These values are comparable to those obtained for Tau^{WT}-mEos3.2 in untreated cells (Fig 2).

Previous studies have described cholesterol-dependent and -independent mechanisms of protein clustering at the plasma

Figure 3. Tau hot spots display distinct motion near the plasma membrane.

A Schematic of the 0N4R Tau isoform carboxy-terminally tagged with HaloTag (Tau^{WT}-HaloTag).

B Representative diffraction-limited image of an N2a cell expressing mEmerald acquired in the green emission channel before single-molecule imaging of Tau^{WT}-HaloTag in the far-red channel.

C–E Intensity map (C), Voronoï diagram (D), and hot spot map (E) of Tau^{WT}-HaloTag molecules corresponding to the boxed region highlighted in (A).

F Representative time series of detections from Tau^{WT}-HaloTag hot spots highlighted in (D).

G, H Distributions of burst duration and size. The mean ± s.d. is shown together with the number of hot spots analyzed in brackets. $n = 13$ cells from $N = 2$ independent experiments.

I Examples of hot spots that are immobile (left) and mobile (right). Top, the localization of hot spots color-coded based on time since hot spot detection. Bottom, trajectories of hot spots constructed by sampling localization belonging to hot spots at 200 ms interval.

J MSDs of Tau^{WT}-HaloTag hot spots with colored curves representing hot spots highlighted in (I).

Source data are available online for this figure.

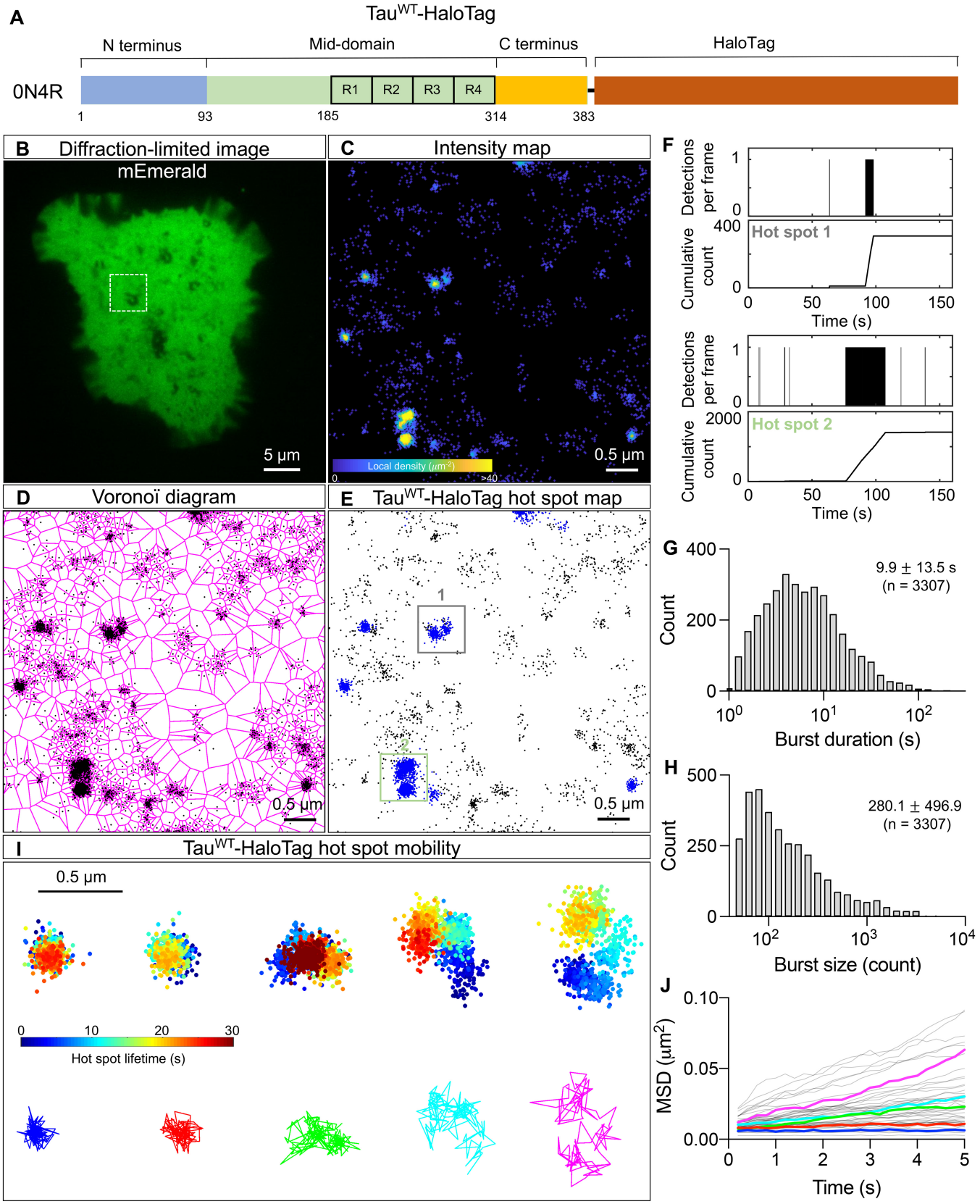
A
Tau^WT-HaloTag
N terminus
Mid-domain
C terminus
HaloTag
0N4R
R1
R2
R3
R4
1
93
185
314
383
B Diffraction-limited image
mEmerald
5 µm
C Intensity map
Local density (µm⁻²)
0
>40
0.5 µm
D Voronoï diagram
0.5 µm
E Tau^WT-HaloTag hot spot map
1
2
0.5 µm
F
Detections per frame
Cumulative count
Hot spot 1
Time (s)
Hot spot 2
G
Count
9.9 ± 13.5 s
(n = 3307)
Burst duration (s)
H
Count
280.1 ± 496.9
(n = 3307)
Burst size (count)
I Tau^WT-HaloTag hot spot mobility
0.5 µm
Hot spot lifetime (s)
J
MSD (µm²)
Time (s)

Figure 3.

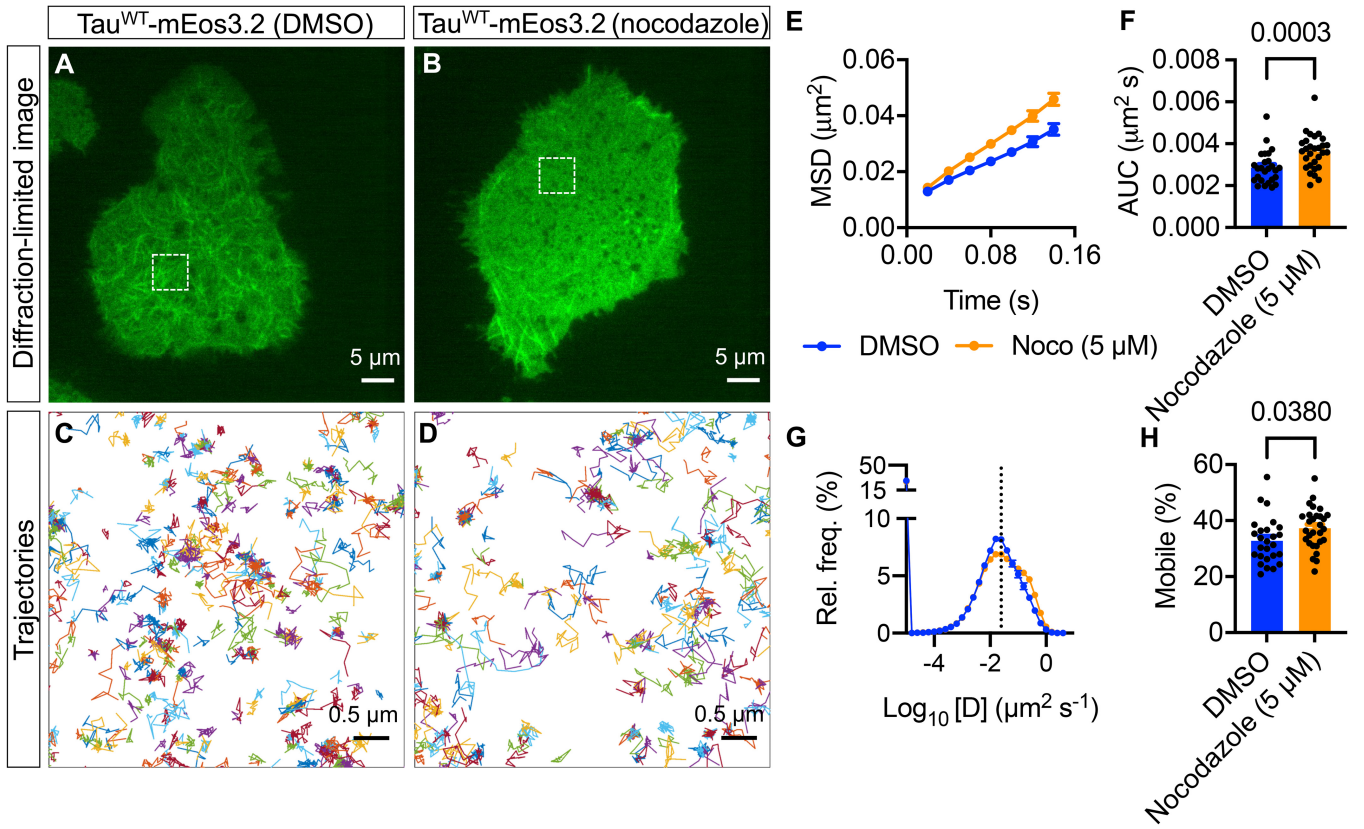

Figure 4. Preventing Tau–microtubule interactions pharmacologically increases the mobility of individual Tau molecules near the plasma membrane.

A, B Representative diffraction-limited TIRF image of N2a cells expressing Tau^{WT}-mEos3.2 treated with either DMSO (A) or 5 μM nocodazole (B) acquired before sptPALM imaging. Scale bar, 5 μm.

C, D Maps of trajectories of Tau^{WT}-mEos3.2 molecules corresponding to the boxed region highlighted in (A) and (B).

E–H Comparison of Tau^{WT}-mEos3.2 mobility parameters in DMSO- and nocodazole-treated live cells. (E, F) Average MSD as a function of time (E) and the corresponding area under the curve (F). (G, H) The distribution of diffusion coefficient (G) shown in semi-log plot and the corresponding mobile fractions (H). Error bars, s.e.m.

Data information: $n = 26$ DMSO-treated and 29 nocodazole-treated cells from $N = 3$ independent experiments. Statistical analysis was performed using the Mann–Whitney U test (F) and the Student's t-test (H).
Source data are available online for this figure.

membrane (Zhou & Hancock, 2015), and cholesterol depletion has been shown to decrease the unconventional release of Tau through the plasma membrane in N2a cells (Merezhko *et al*, 2018). We therefore examined the effect of cholesterol depletion on the dynamics of the Tau hot spots by treating Tau$^{S262E/S356E}$-mEos3.2-expressing N2a cells with 6 mM methyl-β-cyclodextrin (MβCD), a concentration known to strongly deplete cholesterol. Interestingly, there was no apparent effect of cholesterol depletion on the dynamics of the Tau hot spots, with their burst duration, burst size, and density being 13.6 ± 14.6 s, 172.9 ± 338.2 detection counts, and 0.46 ± 0.22 spots/μm^2 (mean ± s.d.), respectively (Fig 6O–U). Together, these findings suggest that Tau hot spots persist after microtubule perturbations and cholesterol depletion.

Discussion

The cytosolic leaflet of the plasma membrane has long been implicated as a site where Tau exerts several of its critical physiological and pathological functions. However, due to the limitations of conventional cell biological techniques, we still lack a comprehensive understanding of this protein's behavior and organization near the plasma membrane of live cells. In this study, we describe how Tau diffuses and organizes near the plasma membrane at single-molecule resolution. Specifically, we identify distinct kinetic subpopulations of Tau in this compartment and demonstrate that Tau forms hot spots, displaying stationary and mobile phases. Moreover, we show that these hot spots last tens of seconds and persist after microtubule perturbations and cholesterol depletion. Together, our study provides fundamental new insight into the complex spatiotemporal organization of Tau near the plasma membrane.

What are the observed Tau hot spots? Previous studies have reported liquid–liquid phase separation of Tau, causing the formation of Tau condensates in solutions (Kanaan *et al*, 2020) and the cytosol of live cells (Wegmann *et al*, 2018). Moreover, in a cell-free system, microtubules have been shown to catalyze Tau condensation and concentrate Tau molecules in focal regions (Siahaan *et al*, 2019; Tan *et al*, 2019). In these studies, Tau condensates in the

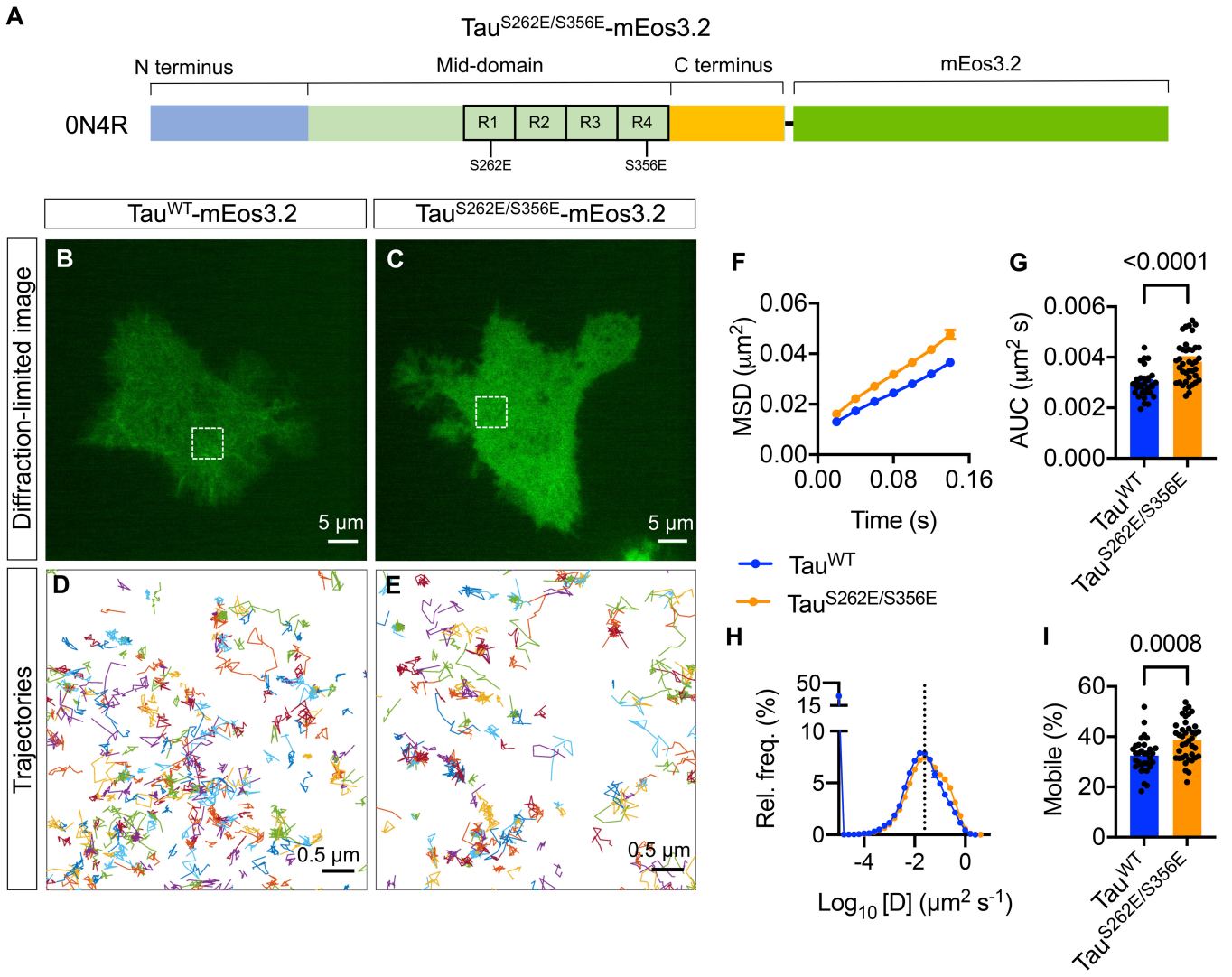

Figure 5. Preventing Tau-microtubule interactions biochemically increases the mobility of individual Tau molecules near the plasma membrane.

A Schematic of 0N4R Tau tagged with mEos3.2 at the C-terminus with S262E/S356E mutations to disrupt microtubule binding.

B, C Representative diffraction-limited TIRF image of a N2a cell expressing Tau^{WT}-mEos3.2 (B) and Tau$^{S262E/S356E}$-mEos3.2 (C).

D, E Maps of trajectories of Tau^{WT}-mEos3.2 and Tau$^{S262E/S356E}$-mEos3.2 molecules corresponding to the box region highlighted in (B) and (C), respectively.

F–I Comparison of Tau^{WT}-mEos3.2 and Tau$^{S262E/S356E}$-mEos3.2 mobility parameters in live cells. (F, G) Average MSD as a function of time (F) and corresponding AUC (G). (H, I) The distribution of diffusion coefficient (H) shown in semi-log plot and the corresponding immobile fraction (I). Error bars, s.e.m.

Data information: $n = 32$ cells expressing Tau^{WT}-mEos3.2 and 39 cells expressing Tau$^{S262E/S356E}$-mEos3.2 from $N = 4$ independent experiments. Statistical analysis was performed using the Student's *t*-test.
Source data are available online for this figure.

cytoplasm or on the microtubules were detectable using conventional diffraction-limited techniques. By contrast, in our cellular system, we did not observe such condensate-like structures near the plasma membrane in our diffraction-limited TIRF images, which revealed either a uniform or microtubule filament-like organization of Tau in this compartment. Importantly, however, we detected Tau hot spots whose sizes were smaller than the diffraction limit (< 250 nm) exclusively in our single-molecule localization microscopy images. In addition, inhibiting Tau/microtubule interactions, using either a microtubule-destabilizing agent or microtubule-binding-deficient mutant, did not abolish the hot spots. These observations suggest that these hot spots may differ from the previously reported Tau condensates. Tau phase separation has been suggested as an intermediate step in the Tau aggregation process. It is tempting to speculate that Tau hot spots and condensates represent different stages in the Tau aggregation pathways. However, whether the hot spots and condensates interconvert or are intermediates in divergent Tau aggregation pathways, some leading to fibrils and others not, remains to be investigated.

Using direct stochastic optical reconstruction microscopy and immunoelectron microscopy of fixed N2a cells, Merezhko *et al* (2018) observed Tau localization in ~ 50–80 nm sized

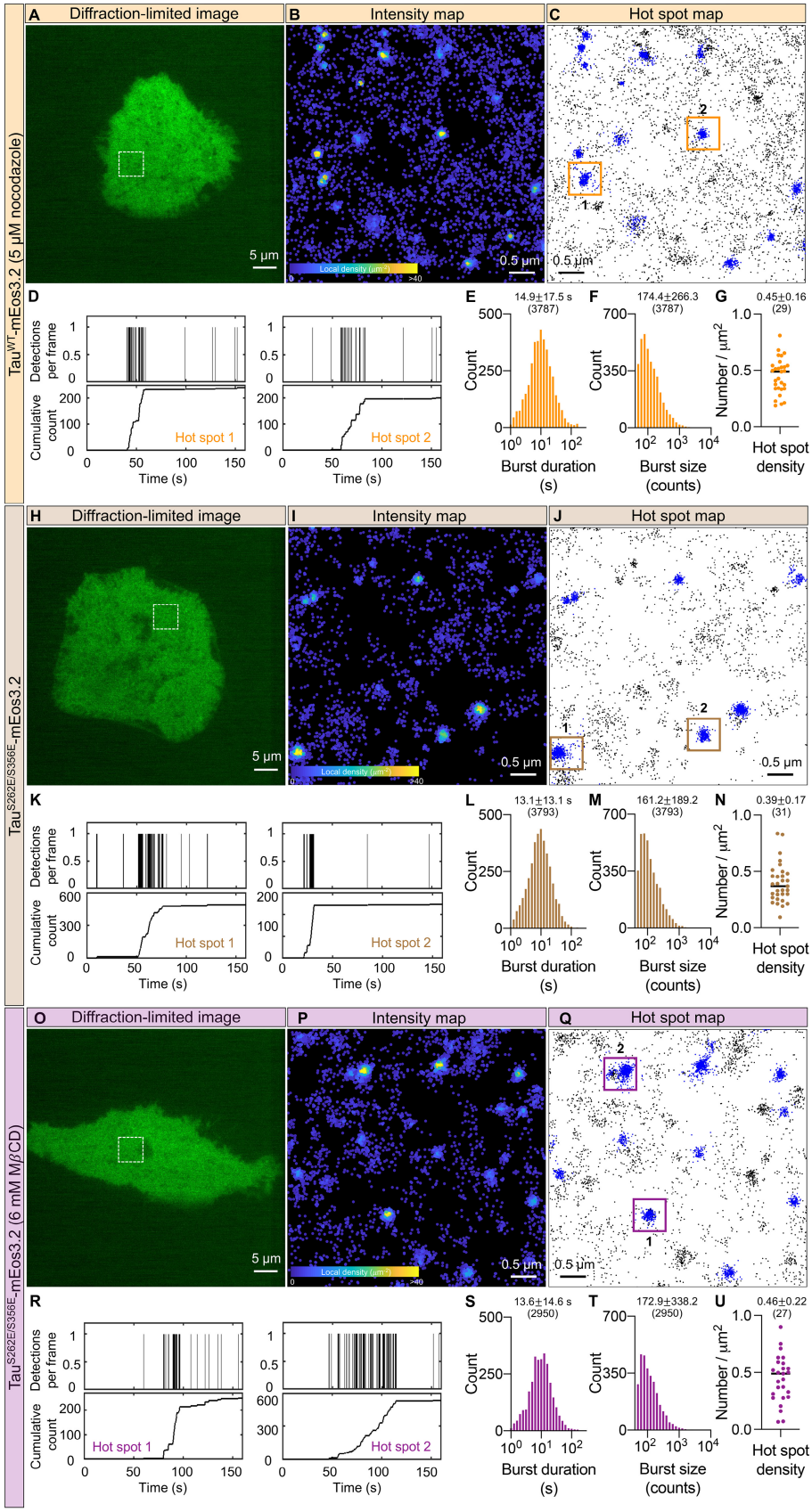

Figure 6.

Figure 6. Tau hot spots near the plasma membrane are resistant to both microtubule perturbation and cholesterol depletion.

A Representative diffraction-limited TIRF image of an N2a cell expressing Tau^{WT}-mEos3.2 in nocodazole-treated live cells.
B, C Maps of intensities (B) and hot spots (C) of Tau^{WT}-mEos3.2 corresponding to the boxed region highlighted in (A).
D Representative time series of detections from Tau^{WT}-mEos3.2 hot spots highlighted in (D).
E, F Distribution of burst duration and size.
G Variations in the density of detected hot spots across cells.
H Representative diffraction-limited TIRF image of an N2a cell expressing $Tau^{S262E/S356E}$-mEos3.2 in live untreated cells.
I, J Maps of intensities (I) and hot spots (J) of $Tau^{S262E/S356E}$-mEos3.2 corresponding to the boxed region highlighted in (H).
K Representative time series of detections from Tau^{WT}-mEos3.2 hot spots highlighted in (H).
L, M Distributions of burst duration and burst size.
N Variations in the density of detected hot spots across cells.
O Representative diffraction-limited TIRF image of an N2a cell expressing $Tau^{S262E/S356E}$-mEos3.2 in live cholesterol-depleted cells.
P, Q Maps of intensities (P) and hot spots (Q) of $Tau^{S262E/S356E}$-mEos3.2 corresponding to the boxed region highlighted in (O).
R Representative time series of detections from Tau^{WT}-mEos3.2 hot spots highlighted in (Q).
S, T The distributions of burst duration and burst size.
U Variations in the density of detected hot spots across cells.

Data information: In (D–G) The analysis corresponds to experiments in Fig 4 ($n = 29$ nocodazole-treated cells from $N = 3$ independent experiments). In (K–N) $n = 31$ cells expressing $Tau^{S262E/S356E}$-mEos3.2 from $N = 4$ independent experiments. In (R–U) $n = 27$ cells expressing $Tau^{S262E/S356E}$-mEos3.2 treated with 6 mM MβCD from $N = 4$ independent experiments. In (E, F, L, M, S, T) the mean ± s.d. is shown together with the number of hot spots analyzed in brackets. In (G, N, U) the mean ± s.d. is shown together with the number of cells analyzed in brackets.
Source data are available online for this figure.

microdomains, which were not enclosed by membrane but were positioned just below the plasma membrane. They suggested that these domains mark the sites of Tau release into the extracellular space. It is therefore plausible that a subset of the hot spots that we observed in live cells using the sptPALM technique represents the Tau microdomains detected in fixed cells. Further, by super-resolution imaging of Tau in fixed cell lines and hippocampal neurons, Gyparaki *et al* (2021) reported the presence of Tau nanoclusters on microtubules. These contained oligomeric Tau and were much smaller than the Tau condensates on microtubules observed in a cell-free system (Siahaan *et al*, 2019). It is likely that in conditions where Tau/microtubule interactions are not perturbed, a subset of Tau hot spots is associated with microtubules. Determining whether the Tau hot spots in live cells and the Tau nanoclusters in fixed cells represent the same or different entities will be an important subject for future research.

How do the observed hot spots form? Protein clustering has emerged as a dominant feature of cellular organization (Padmanabhan *et al*, 2020, 2021). Interestingly, the dynamics of Tau hot spots near the plasma membrane that we observed resembled that of membrane receptor clusters (Gormal *et al*, 2020) and intracellular RNA polymerase II clusters (Cisse *et al*, 2013; Wei *et al*, 2020). Protein clusters can form either through self-association or interaction with binding partners. Therefore, one possibility is that preexisting plasma membrane-associated clusters of Tau's interaction partner(s), such as Fyn and annexin, may serve as hubs to capture and trap Tau molecules as they pass by. Considering that many membrane lipids interact with Tau (Bok *et al*, 2021; Sallaberry *et al*, 2021) and that anionic compounds such as arachidonic acid, which are present in these lipids, promote Tau nucleation in a cell-free system (King *et al*, 2000), Tau/lipid interactions at the plasma membrane could possibly generate assemblies that resemble the Tau hot spots observed in our study. Alternatively, Tau might itself form assemblies at the plasma membrane and interact with membrane-associated proteins and lipids. Previous studies have shown that different recombinant forms of Tau have different aggregation rates and filament formation capabilities in cell-free conditions (Goedert & Jakes, 1990; King *et al*, 2000). For instance, in the presence of arachidonic acid, Tau isoforms (0N3R and 0N4R) lacking N-terminal exons 2 and 3 aggregate into smaller, globular oligomers, whereas those (1N3R and 2N3R) containing these exons form very long filaments (King *et al*, 2000). Moreover, missense mutations found in frontotemporal lobar degeneration (FTLD), such as P301L and R406W, exert differential effects on Tau aggregation kinetics and accelerate the aggregation of Tau into filaments (Nacharaju *et al*, 1999; Mutreja *et al*, 2019). How this is reflected *in vivo* and whether different isoforms and FTDP-17 mutations have distinct hot spot dynamics remain to be investigated. Future work is therefore needed to determine how different factors work together to regulate the dynamics of Tau hot spots.

What could be the functions of these hot spots? An intriguing possibility is that they are the sites where vesicle-free Tau is released into the extracellular space (Katsinelos *et al*, 2018; Merezhko *et al*, 2018). Given that Tau interacts with actin and microtubules (Magnani *et al*, 2007), it is also plausible that hot spot formation is necessary for Tau to link the cytoskeleton to the plasma membrane. Alternatively, Tau hot spots could be molecular depots that recruit specific membrane-associated molecules to regulate signaling pathways in a local environment (Li & Götz, 2017; Mueller *et al*, 2021). An exciting next step forward would therefore be to characterize the local environment (such as lipid and protein composition) that influences or is influenced by Tau hot spots and to determine the functions of Tau hot spots.

Another interesting observation of our study is that the burst duration (apparent lifetime) of the hot spots varied by up to two orders of magnitude for all tested conditions, indicating that there is substantial variability in the kinetics of the hot spots and that multiple mechanisms may determine their formation and stability. Remarkably, the lifetime of a hot spot far exceeds the reported ~ 40 ms dwell time of Tau on microtubules (Janning *et al*, 2014), hinting at the possibility that the interactions of Tau with different partners lead to vastly different Tau behaviors and potentially different biological outcomes. It is tempting to speculate that it is not only the dynamics of individual hot spots but also the coordination of

multiple hot spots at the plasma membrane that determines the membrane functions of Tau. Whether Tau hot spots contribute to membrane insertion and fibrillization in pathological conditions such as Alzheimer's disease remains to be determined.

Protein motion types have previously been linked to conformational changes, protein–protein interactions, and post-translation modifications. Here, we show that Tau, a protein that undergoes extensive post-translation modifications, exhibits distinct motion states; it undergoes free diffusion along the plasma membrane, becomes immobilized and trapped inside hot spots, and can be bound and transiently confined by microtubules. In our study, the diffusion coefficient of Tau varied over several orders of magnitude, suggesting that multiple mechanisms might underlie the heterogenous mobility patterns of Tau near the plasma membrane. Given that a significant fraction of Tau molecules diffuses freely near the plasma membrane, we speculate that free diffusion is a strategy that allows Tau to explore the membrane at high efficiency, and that this pool serves as a reservoir to supply Tau to its multiple interactors at the plasma membrane. Consistent with this notion, blocking the interactions of Tau with its partner microtubules increases the mobile reservoir pool of Tau available for other interactions. This dynamic property of Tau likely allows the protein to transiently interact with multiple partners and thereby execute a rich repertoire of cellular functions in space and time (Pooler *et al*, 2012; Croft *et al*, 2017).

We recognize the limitations of our study. Firstly, our approach relies on transient overexpression of Tau in N2a and HEK293T cell lines. However, using the intensity of the cell footprint as a proxy for Tau expression, we did not image cells with very high expression levels. Secondly, although we have used different tags (mEos3.2 and HaloTag) to investigate the dynamic behavior of Tau, the possibility of a role of the tag in Tau hot spot assembly and stability cannot be fully ruled out. Addressing these limitations would require the development of novel molecular and imaging tools to quantify the dynamics of label-free, endogenous Tau in live cells. Finally, because the width of the plasma membrane is < 10 nm, which is much smaller than the ~ 100 nm axial resolution of TIRF illumination, it is not possible to determine whether the Tau hot spots associate directly with the plasma membrane or are linked indirectly through other proteins or structures. Further work with an improved axial resolution is needed to clarify the precise location of these hot spots in this compartment.

In summary, our study sheds new light on the spatiotemporal organization of Tau near the plasma membrane. Given Tau's emerging role as a multifunctional protein in physiology and pathology, we provide a framework to investigate the functions of Tau at the plasma membrane and in other cellular compartments.

Materials and Methods

Cell culture and transfection

N2a mouse neuroblastoma cells were maintained in Dulbecco's minimum essential medium (ThermoFisher; Catalog No. 11965-092) supplemented with 10% fetal bovine serum (Bovogen; Catalog No. SFBS-F) and 50 U/ml penicillin/streptomycin (Gibco; Catalog No. 15140-122). Cells were tested for mycoplasma and were not authenticated before use. Cells were grown at 37°C in 5% CO_2. 250,000 cells per well were plated in 12-well plates for 18 h before transfection. Lipofectamine™ LTX and Plus reagent (Invitrogen; Catalog No. 15338030) were used for cell transfections as per the manufacturer's instructions. For imaging, the cells were dissociated with Trypsin–EDTA (0.25%; Catalog No. 25200-056), centrifuged, and $\sim$ 32,000 cells replated on poly-D-lysine-coated 35 mm glass-bottom culture dishes (Ibidi) for 1–2 h. The medium was then fully changed, and cells were imaged after 16–40 h.

Plasmids

Mammalian expression plasmids were made using human tau cDNA for isoform 0N4R and the human cytomegalovirus (CMV) promoter. Fusion proteins were created with a C-terminal tag of mEos3.2, HaloTag, or FLAG-tag (DYKDDDDK). The plasmid mEos3.2-C1 was a gift from Michael Davidson and Tao Xu (RRID:Addgene #54550) (Zhang *et al*, 2012). Pseudophosphorylated Tau at Ser262 and Ser356 was made by substitution of serine with glutamic acid. Plasmids for control expression of tagged proteins were created by deletion of the tau encoding sequence.

Western blot analysis

N2a cells were collected for expression validation from the 12-well plate at 24 h post-transfection in RIPA buffer (Cell Signaling Technologies; Catalog No. 9806) in the presence of phosphatase inhibitor (Roche; Catalog No. 04906837001) and protease inhibitor (Roche; Catalog No. 04693159001). Samples were diluted in Laemmli buffer, sonicated, and heated to 95°C for 10 min, then separated using SDS–PAGE on 4–20% Criterion TGX (BioRad; Catalog Nos. 5671084 and 5671085) gradient gels at 250 V. The samples were transferred to nitrocellulose membranes (Merck; Catalog No. HATF00010) for 50 min at 400 mA. The membranes were then blocked in TBS containing Odyssey Blocking Buffer (LI-COR; Catalog No.927-50000) and incubated in primary antibodies (Tau5 1:5,000) overnight at 4°C followed by incubation with the secondary antibody for one hour at room temperature. Membranes were imaged on the LI-COR Odyssey scanner using the Image Studio software (LI-COR; Catalog Nos. 926-32211 and 926-68070).

TIRF microscopy and single-molecule imaging

For live-cell TIRF microscopy, transfected cells were imaged using an iLas^2 azimuthal TIRF illumination system (Roper Scientific) mounted on a Nikon Ti-E inverted microscope, with a 100×/1.49 NA oil-immersion TIRF objective (CFI Apochromat, Nikon) and Evolve 512 Delta EMCCD cameras (Teledyne Photometrics). Image acquisition was performed using MetaMorph (version 7.10.1.161, Molecular Devices). Single-molecule imaging of Tau tagged with mEos3.2 was performed at 50 Hz to record 8,000 frames per cell at 37°C. Cells were washed and incubated with buffer A (145 mM NaCl, 5 mM KCl, 1.2 mM Na_2HPO_4, 10 mM D-glucose, 20 mM Hepes, pH 7.4) during imaging. To perform sptPALM, we used a 405 nm laser (Stradus 405, Vortran Laser Technology) to photoconvert the mEos3.2-tagged molecules and a 561 nm laser (Cobolt Jive, Cobolt Lasers) for excitation of the photoconverted molecules. To activate and detect the mEos3.2 signal from the background signals,

we used a TIRFM GFP/RFP filter cube (Nikon Corporation) in the microscope body, a T565lpxr long-pass dichroic beam splitter, and an ET600/50 m emission filter (Chroma Technology) in the TwinCam (Cairn Research) dual emission image splitter transmission arm. The 405 nm laser power density was between 3.4×10^{-6} and 9.5×10^{-5} kW/cm^2, and the 561 nm laser power density was set to ~ 0.14 kW/cm^2. To track Tau^{WT}-HaloTag, we first incubated cells co-expressing Tau^{WT}-HaloTag and the cell fill mEmerald with the Halo ligand (2 pM) for 15 min at 37°C. The cells were then washed and Tau^{WT}-HaloTag molecules were tracked using a 642 nm laser at a power density of 0.12 kW/cm^2, a ZT405/488/561/647rpc quad-band dichroic beam splitter, and a ZET405/488/561/640m emission filter (Chroma Technology) in the microscope body, and a ZT647rdc dichroic beam splitter and an ET690/50m emission filter (Chroma Technology) in the TwinCam transmission arm.

Nocodazole and MβCD treatments

For nocodazole treatment experiments, cells were incubated with either nocodazole (5 μM) or DMSO mixed with a culture medium. Cells were then washed and incubated with buffer A containing either nocodazole (5 μM) or DMSO during imaging. For MβCD experiments, cells were washed and incubated with buffer A containing 6 mM MβCD. Imaging was performed between 5 and 40 min after MβCD treatment.

SptPALM analysis

Tracking

We localized and tracked individual Tau molecules tagged with mEos3.2 as previously described (Joensuu *et al*, 2016, 2017; Bademosi *et al*, 2017; Padmanabhan *et al*, 2019). Briefly, individual molecules were localized using a wavelet-based segmentation algorithm (Izeddin *et al*, 2012), and trajectories were computed using a simulated annealing-based tracking algorithm (Racine *et al*, 2006), with the PALM-Tracer tool that operates as a plugin of Metamorph software (Molecular Devices). We used a frame-to-frame particle-linking distance threshold of 318 nm (3 pixels) and visually inspected for misconnections using the InferenceMAP tool in both fixed and live cells (El Beheiry *et al*, 2015). Cells with at least 500 Tau-mEos3.2 trajectories were used for further analysis. Of note, we observed a small proportion of mobile molecules in fixed samples, potentially due to incomplete molecular immobilization after fixation using paraformaldehyde (Tanaka *et al*, 2010).

Intensity and trajectory maps

Intensity and trajectory maps were constructed using detections lasting at least four and eight consecutive frames, respectively. For intensity maps, the local density of each detection was determined by computing the number of detections with a circle of 30 nm radius using a custom-written code.

Mean square displacement and diffusion coefficients

We constructed trajectories of detections that lasted at least eight consecutive frames and computed the MSD of each trajectory. The MSD was fitted by the equation $MSD(\tau) = a + 4D\tau$, where D is the diffusion coefficient, a is the y-intercept and τ is the time shift. Trajectories lasting at least eight frames were considered for analysis of MSD and diffusion coefficients. The average MSD of all trajectories from each analyzed cell was fitted by the equation $MSD(\tau) = a + 4D_{avg}\tau$ to estimate the average diffusion coefficient D_{avg} (Appendix Fig S12).

Moment scaling spectrum

Using the divide-and-conquer moment scaling spectrum (DC-MSS) tool (Vega *et al*, 2018), we performed an MSS analysis of Tau^{WT}-mEos3.2 trajectories that lasted at least 20 frames, estimated the slope of MSS, and categorized the trajectories into different motion states, as described previously (Jaqaman *et al*, 2011; Vega *et al*, 2018). Briefly, for every time shift τ, the moments of displacement, μ_m, were computed for $m = 1, \ldots, 6$. Next, using the relationship $\mu_m(\tau) = 4D_m\tau^{\alpha m}$, the generalized diffusion coefficient D_m and the exponent α_m were estimated for each m. The plot α_m versus m yielded the MSS and the slope of the MSS allowed categorization of the trajectories into different motion types.

Hidden Markov modeling

The vibrational Bayes SPT (vbSPT) tool (Persson *et al*, 2013) was used to analyze Tau^{WT}-mEos3.2 and Tau$^{S262E/S356E}$-mEos3.2 trajectories. Cells with ≥ 1,000 trajectories were used for this analysis. The HMM approach models the trajectories as random transitions between a set of hidden states with different diffusion coefficients. By applying Bayesian model selection to hidden Markov models, the vbSPT analysis infers the number of hidden diffusive states and the associated parameters from the experimental data. When we initially allowed a maximum of 10 hidden states, models with 2–7 states provided the best fit (Appendix Fig S5), indicating a heterogeneous mobility pattern of Tau near the plasma membrane. We have presented the parameters estimated by fitting a three-state model to the experimental data (Fig 1L; Appendix Figs S5F, S6J, and S11B).

Frame-to-frame displacement analysis

We computed the empirical cumulative frequency distribution of the displacements of Tau molecules tagged with mEos3.2 molecules at 20 ms intervals using the tool ECDF in MATLAB. The one-state model is described by $C(r,\Delta t) = 1 - f_1 \exp\left(\frac{-r^2}{4D_1\Delta t}\right)$, the two-state model by $C(r,\Delta t) = 1 - f_1 \exp\left(\frac{-r^2}{4D_1\Delta t}\right) - f_2 \exp\left(\frac{-r^2}{4D_2\Delta t}\right)$, and the three-state model by $C(r,\Delta t) = 1 - f_1 \exp\left(\frac{-r^2}{4D_1\Delta t}\right) - f_2 \exp\left(\frac{-r^2}{4D_2\Delta t}\right) - f_3 \exp\left(\frac{-r^2}{4D_3\Delta t}\right)$. Here, r is the displacement, Δt is the time interval (20 ms), D_1, D_2 and D_3 are the diffusion coefficients of the three states, and f_1, f_2, and f_3 are the state occupancies. We fit the predictions of different models to the data using the nonlinear regression tool NLINFIT in MATLAB to estimate the model parameters.

Voronoÿ tessellation and time-correlated PALM (tcPALM)

We used a cross-correlation-based method to correct for any motion drift during imaging acquisition (Andronov *et al*, 2016). We then used the SR-Tesseler tool (Levet *et al*, 2015) to identify the outline of the cell (object). Tau hot spots were identified as regions with a local density at least five-fold greater than the average density of the object. Next, we performed the tcPALM analysis (Cisse *et al*, 2013; Cho *et al*, 2018) by drawing a square region of interest around each spot and computing the number of

detections within the region as a function of time. The start and end points of each burst were identified from the cumulative detections using a dark time tolerance, Tol, of 200 frames. Bursts with at least 50 detections (minimum burst size, MinB = 50) were considered for further analysis. We tested the sensitivity of burst duration and size by varying Tol and MinB (Appendix Fig S13) and the sensitivity of burst size to multiple single-molecule appearances (Appendix Fig S14). To avoid cell edge confounds due to the folding of membranes at the edges, we analyzed cell areas of $\sim$ 100–400 μm^2, excluding cell edges.

Statistical analysis

The D'Agostino and Pearson test was used to test for normality, and the Student's *t*-test was used for statistical comparison when the data were normally distributed. Otherwise, the Mann–Whitney *U* test was employed. When data sets had more than two groups, an ANOVA was used with appropriate corrections for multiple comparisons. No statistical methods were used to predetermine the sample size, no randomization procedures were employed, and investigators were not blinded during data acquisition and analysis. Values are represented as the mean $\pm$ s.e.m or mean $\pm$ s.d., as indicated in the figure legends. Data were considered significant at $P < 0.05$. GraphPad Prism 9 was used to perform statistical tests.

Data availability

This study includes no data deposited in a database. All data associated with this study are available within the manuscript and its Appendix Information.

Expanded View for this article is available online.

Acknowledgements
We thank Rowan Tweedale for the critical reading of the manuscript. We acknowledge Corey Butler and Adel Kechkar for their contributions to the development of PALM-Tracer. The imaging was performed at the Queensland Brain Institute Advanced Microscopy Facility, supported by the Australian Government through an Australian Research Council LIEF grant (LE130100078). We acknowledge support from the Estate of Dr. Clem Jones, the State Government of Queensland (DSITI, Department of Science, Information Technology and Innovation), and the National Health and Medical Research Council of Australia (GNT1176326 and GA39196) to JG. Open access publishing facilitated by The University of Queensland, as part of the Wiley - The University of Queensland agreement via the Council of Australian University Librarians.

Author contributions
Pranesh Padmanabhan: Conceptualization; data curation; software; formal analysis; validation; investigation; visualization; methodology; writing – original draft; project administration; writing – review and editing. **Andrew Kneynsberg:** Conceptualization; resources; investigation; writing – review and editing. **Esteban Cruz:** Resources; investigation; writing – review and editing. **Rumelo Amor:** Methodology; writing – review and editing. **Jean-Baptiste Sibarita:** Software; methodology; writing – review and editing. **Jürgen Götz:** Conceptualization; funding acquisition; investigation; writing – original draft; project administration; writing – review and editing.

Disclosure and competing interests statement
The authors declare that they have no conflict of interest.

References

Andronov L, Lutz Y, Vonesch JL, Klaholz BP (2016) SharpViSu: integrated analysis and segmentation of super-resolution microscopy data. *Bioinformatics* 32: 2239–2241

Arrasate M, Pérez M, Avila J (2000) Tau dephosphorylation at tau-1 site correlates with its association to cell membrane. *Neurochem Res* 25: 43–50

Bademosi AT, Lauwers E, Padmanabhan P, Odierna L, Chai YJ, Papadopulos A, Goodhill GJ, Verstreken P, van Swinderen B, Meunier FA (2017) *In vivo* single-molecule imaging of syntaxin1A reveals polyphosphoinositide- and activity-dependent trapping in presynaptic nanoclusters. *Nat Commun* 8: 13660

Boimel M, Grigoriadis N, Lourbopoulos A, Touloumi O, Rosenmann D, Abramsky O, Rosenmann H (2009) Statins reduce the neurofibrillary tangle burden in a mouse model of tauopathy. *J Neuropathol Exp Neurol* 68: 314–325

Bok E, Leem E, Lee BR, Lee JM, Yoo CJ, Lee EM, Kim J (2021) Role of the lipid membrane and membrane proteins in tau pathology. *Front Cell Dev Biol* 9: 653815

Braak H, Del Tredici K (2011) Alzheimer's pathogenesis: is there neuron-to-neuron propagation? *Acta Neuropathol* 121: 589–595

Brandt R, Leger J, Lee G (1995) Interaction of tau with the neural plasma membrane mediated by Tau's amino-terminal projection domain. *J Cell Biol* 131: 1327–1340

Brandt R, Trushina NI, Bakota L (2020) Much more than a cytoskeletal protein: physiological and pathological functions of the non-microtubule binding region of tau. *Front Neurol* 11: 590059

Caceres A, Kosik KS (1990) Inhibition of neurite polarity by tau antisense oligonucleotides in primary cerebellar neurons. *Nature* 343: 461–463

Chang CW, Shao E, Mucke L (2021) Tau: enabler of diverse brain disorders and target of rapidly evolving therapeutic strategies. *Science* 371: eabb8255

Chen YM, Wang QJ, Hu HS, Yu PC, Zhu J, Drewes G, Piwnica-Worms H, Luo ZG (2006) Microtubule affinity-regulating kinase 2 functions downstream of the PAR-3/PAR-6/atypical PKC complex in regulating hippocampal neuronal polarity. *Proc Natl Acad Sci USA* 103: 8534–8539

Cho WK, Spille JH, Hecht M, Lee C, Li C, Grube V, Cisse II (2018) Mediator and RNA polymerase II clusters associate in transcription-dependent condensates. *Science* 361: 412–415

Cisse II, Izeddin I, Causse SZ, Boudarene L, Senecal A, Muresan L, Dugast-Darzacq C, Hajj B, Dahan M, Darzacq X (2013) Real-time dynamics of RNA polymerase II clustering in live human cells. *Science* 341: 664–667

Croft CL, Wade MA, Kurbatskaya K, Mastrandreas P, Hughes MM, Phillips EC, Pooler AM, Perkinton MS, Hanger DP, Noble W (2017) Membrane association and release of wild-type and pathological tau from organotypic brain slice cultures. *Cell Death Dis* 8: e2671

Dixit R, Ross JL, Goldman YE, Holzbaur EL (2008) Differential regulation of dynein and kinesin motor proteins by tau. *Science* 319: 1086–1089

El Beheiry M, Dahan M, Masson JB (2015) InferenceMAP: mapping of single-molecule dynamics with Bayesian inference. *Nat Methods* 12: 594–595

Elbaum-Garfinkle S, Ramlall T, Rhoades E (2010) The role of the lipid bilayer in tau aggregation. *Biophys J* 98: 2722–2730

Evans HT, Benetatos J, van Roijen M, Bodea LG, Götz J (2019) Decreased synthesis of ribosomal proteins in tauopathy revealed by non-canonical amino acid labelling. *EMBO J* 38: e101174

Evans HT, Taylor D, Kneynsberg A, Bodea LG, Götz J (2021) Altered ribosomal function and protein synthesis caused by tau. *Acta Neuropathol Commun* 9: 110

Fanni AM, Vander Zanden CM, Majewska PV, Majewski J, Chi EY (2019) Membrane-mediated fibrillation and toxicity of the tau hexapeptide PHF6. *J Biol Chem* 294: 15304–15317

Flach K, Hilbrich I, Schiffmann A, Gärtner U, Krüger M, Leonhardt M, Waschipky H, Wick L, Arendt T, Holzer M (2012) Tau oligomers impair artificial membrane integrity and cellular viability. *J Biol Chem* 287: 43223–43233

Garcia-Parajo MF, Cambi A, Torreno-Pina JA, Thompson N, Jacobson K (2014) Nanoclustering as a dominant feature of plasma membrane organization. *J Cell Sci* 127: 4995–5005

Gauthier-Kemper A, Weissmann C, Golovyashkina N, Sebo-Lemke Z, Drewes G, Gerke V, Heinisch JJ, Brandt R (2011) The frontotemporal dementia mutation R406W blocks tau's interaction with the membrane in an annexin A2-dependent manner. *J Cell Biol* 192: 647–661

Georgieva ER, Xiao S, Borbat PP, Freed JH, Eliezer D (2014) Tau binds to lipid membrane surfaces via short amphipathic helices located in its microtubule-binding repeats. *Biophys J* 107: 1441–1452

Goedert M, Jakes R (1990) Expression of separate isoforms of human tau protein: correlation with the tau pattern in brain and effects on tubulin polymerization. *EMBO J* 9: 4225–4230

Gormal RS, Padmanabhan P, Kasula R, Bademosi AT, Coakley S, Giacomotto J, Blum A, Joensuu M, Wallis TP, Lo HP *et al* (2020) Modular transient nanoclustering of activated β2-adrenergic receptors revealed by single-molecule tracking of conformation-specific nanobodies. *Proc Natl Acad Sci USA* 117: 30476–30487

Gura Sadovsky R, Brielle S, Kaganovich D, England JL (2017) Measurement of rapid protein diffusion in the cytoplasm by photo-converted intensity profile expansion. *Cell Rep* 18: 2795–2806

Gyparaki MT, Arab A, Sorokina EM, Santiago-Ruiz AN, Bohrer CH, Xiao J, Lakadamyali M (2021) Tau forms oligomeric complexes on microtubules that are distinct from tau aggregates. *Proc Natl Acad Sci USA* 118: e2021461118

Izeddin I, Boulanger J, Racine V, Specht CG, Kechkar A, Nair D, Triller A, Choquet D, Dahan M, Sibarita JB (2012) Wavelet analysis for single molecule localization microscopy. *Opt Express* 20: 2081–2095

Izeddin I, Récamier V, Bosanac L, Cissé II, Boudarene L, Dugast-Darzacq C, Proux F, Bénichou O, Voituriez R, Bensaude O *et al* (2014) Single-molecule tracking in live cells reveals distinct target-search strategies of transcription factors in the nucleus. *eLife* 3: e02230

Jacobson K, Liu P, Lagerholm BC (2019) The lateral organization and mobility of plasma membrane components. *Cell* 177: 806–819

Janning D, Igaev M, Sundermann F, Bruhmann J, Beutel O, Heinisch JJ, Bakota L, Piehler J, Junge W, Brandt R (2014) Single-molecule tracking of tau reveals fast kiss-and-hop interaction with microtubules in living neurons. *Mol Biol Cell* 25: 3541–3551

Jaqaman K, Kuwata H, Touret N, Collins R, Trimble WS, Danuser G, Grinstein S (2011) Cytoskeletal control of CD36 diffusion promotes its receptor and signaling function. *Cell* 146: 593–606

Joensuu M, Padmanabhan P, Durisic N, Bademosi AT, Cooper-Williams E, Morrow IC, Harper CB, Jung W, Parton RG, Goodhill GJ *et al* (2016) Subdiffractional tracking of internalized molecules reveals heterogeneous motion states of synaptic vesicles. *J Cell Biol* 215: 277–292

Joensuu M, Martinez-Marmol R, Padmanabhan P, Glass NR, Durisic N, Pelekanos M, Mollazade M, Balistreri G, Amor R, Cooper-White JJ *et al* (2017) Visualizing endocytic recycling and trafficking in live neurons by subdiffractional tracking of internalized molecules. *Nat Protoc* 12: 2590–2622

Kanaan NM, Morfini GA, LaPointe NE, Pigino GF, Patterson KR, Song Y, Andreadis A, Fu Y, Brady ST, Binder LI (2011) Pathogenic forms of tau inhibit kinesin-dependent axonal transport through a mechanism involving activation of axonal phosphotransferases. *J Neurosci* 31: 9858–9868

Kanaan NM, Hamel C, Grabinski T, Combs B (2020) Liquid-liquid phase separation induces pathogenic tau conformations *in vitro*. *Nat Commun* 11: 2809

Katsinelos T, Zeitler M, Dimou E, Karakatsani A, Muller HM, Nachman E, Steringer JP, Ruiz de Almodovar C, Nickel W, Jahn TR (2018) Unconventional secretion mediates the trans-cellular spreading of tau. *Cell Rep* 23: 2039–2055

King ME, Gamblin TC, Kuret J, Binder LI (2000) Differential assembly of human tau isoforms in the presence of arachidonic acid. *J Neurochem* 74: 1749–1757

Knops J, Kosik KS, Lee G, Pardee JD, Cohen-Gould L, McConlogue L (1991) Overexpression of tau in a nonneuronal cell induces long cellular processes. *J Cell Biol* 114: 725–733

Kühn T, Ihalainen TO, Hyväluoma J, Dross N, Willman SF, Langowski J, Vihinen-Ranta M, Timonen J (2011) Protein diffusion in mammalian cell cytoplasm. *PLoS One* 6: e22962

Lee Y, Phelps C, Huang T, Mostofian B, Wu L, Zhang Y, Tao K, Chang YH, Stork PJ, Gray JW *et al* (2019) High-throughput, single-particle tracking reveals nested membrane domains that dictate KRas (G12D) diffusion and trafficking. *eLife* 8: e46393

Levet F, Hosy E, Kechkar A, Butler C, Beghin A, Choquet D, Sibarita JB (2015) SR-Tesseler: a method to segment and quantify localization-based super-resolution microscopy data. *Nat Methods* 12: 1065–1071

Li C, Götz J (2017) Somatodendritic accumulation of tau in Alzheimer's disease is promoted by Fyn-mediated local protein translation. *EMBO J* 36: 3120–3138

Magnani E, Fan J, Gasparini L, Golding M, Williams M, Schiavo G, Goedert M, Amos LA, Spillantini MG (2007) Interaction of tau protein with the dynactin complex. *EMBO J* 26: 4546–4554

Majewski J, Jones EM, Vander Zanden CM, Biernat J, Mandelkow E, Chi EY (2020) Lipid membrane templated misfolding and self-assembly of intrinsically disordered tau protein. *Sci Rep* 10: 13324

Manley S, Gillette JM, Patterson GH, Shroff H, Hess HF, Betzig E, Lippincott-Schwartz J (2008) High-density mapping of single-molecule trajectories with photoactivated localization microscopy. *Nat Methods* 5: 155–157

Mari SA, Wegmann S, Tepper K, Hyman BT, Mandelkow EM, Mandelkow E, Müller DJ (2018) Reversible cation-selective attachment and self-assembly of human tau on supported brain lipid membranes. *Nano Lett* 18: 3271–3281

Mehidi A, Rossier O, Schaks M, Chazeau A, Biname F, Remorino A, Coppey M, Karatas Z, Sibarita JB, Rottner K *et al* (2019) Transient activations of Rac1 at the lamellipodium tip trigger membrane protrusion. *Curr Biol* 29: e5

Merezhko M, Brunello CA, Yan X, Vihinen H, Jokitalo E, Uronen RL, Huttunen HJ (2018) Secretion of tau via an unconventional non-vesicular mechanism. *Cell Rep* 25: e4

Mueller RL, Combs B, Alhadidy MM, Brady ST, Morfini GA, Kanaan NM (2021) Tau: a signaling hub protein. *Front Mol Neurosci* 14: 647054

Mutreja Y, Combs B, Gamblin TC (2019) FTDP-17 mutations alter the aggregation and microtubule stabilization propensity of tau in an isoform-specific fashion. *Biochemistry* 58: 742–754

Nacharaju P, Lewis J, Easson C, Yen S, Hackett J, Hutton M, Yen SH (1999) Accelerated filament formation from tau protein with specific FTDP-17 missense mutations. *FEBS Lett* 447: 195–199

Padmanabhan P, Martinez-Marmol R, Xia D, Götz J, Meunier FA (2019) Frontotemporal dementia mutant tau promotes aberrant Fyn nanoclustering in hippocampal dendritic spines. *eLife* 8: e45040

Padmanabhan P, Bademosi AT, Kasula R, Lauwers E, Verstreken P, Meunier FA (2020) Need for speed: super-resolving the dynamic nanoclustering of syntaxin-1 at exocytic fusion sites. *Neuropharmacology* 169: 107554

Padmanabhan P, Kneynsberg A, Götz J (2021) Super-resolution microscopy: a closer look at synaptic dysfunction in Alzheimer disease. *Nat Rev Neurosci* 22: 723–740

Patel N, Ramachandran S, Azimov R, Kagan BL, Lal R (2015) Ion channel formation by tau protein: implications for Alzheimer's disease and tauopathies. *Biochemistry* 54: 7320–7325

Persson F, Lindén M, Unoson C, Elf J (2013) Extracting intracellular diffusive states and transition rates from single-molecule tracking data. *Nat Methods* 10: 265–269

Polanco JC, Li C, Bodea LG, Martinez-Marmol R, Meunier FA, Götz J (2018) Amyloid-β and tau complexity - towards improved biomarkers and targeted therapies. *Nat Rev Neurol* 14: 22–39

Polanco JC, Hand GR, Briner A, Li C, Götz J (2021) Exosomes induce endolysosomal permeabilization as a gateway by which exosomal tau seeds escape into the cytosol. *Acta Neuropathol* 141: 235–256

Pooler AM, Usardi A, Evans CJ, Philpott KL, Noble W, Hanger DP (2012) Dynamic association of tau with neuronal membranes is regulated by phosphorylation. *Neurobiol Aging* 33: 431

Racine V, Hertzog A, Jouanneau J, Salamero J, Kervrann C, Sibarita J-B (2006) Multiple-target tracking of 3D fluorescent objects based on simulated annealing. In *IEEE International Symposium on Biomedical Imaging: Macro to Nano*, Vol. 1–3, pp 1020–1023. Arlington, VA: IEEE

Rossier O, Octeau V, Sibarita JB, Leduc C, Tessier B, Nair D, Gatterdam V, Destaing O, Albigès-Rizo C, Tampé R *et al* (2012) Integrins β1 and β3 exhibit distinct dynamic nanoscale organizations inside focal adhesions. *Nat Cell Biol* 14: 1057–1067

Sallaberry CA, Voss BJ, Majewski J, Biernat J, Mandelkow E, Chi EY, Vander Zanden CM (2021) Tau and membranes: interactions that promote folding and condensation. *Front Cell Dev Biol* 9: 725241

Siahaan V, Krattenmacher J, Hyman AA, Diez S, Hernandez-Vega A, Lansky Z, Braun M (2019) Kinetically distinct phases of tau on microtubules regulate kinesin motors and severing enzymes. *Nat Cell Biol* 21: 1086–1092

Tan R, Lam AJ, Tan T, Han J, Nowakowski DW, Vershinin M, Simo S, Ori-McKenney KM, McKenney RJ (2019) Microtubules gate tau condensation to spatially regulate microtubule functions. *Nat Cell Biol* 21: 1078–1085

Tanaka KA, Suzuki KG, Shirai YM, Shibutani ST, Miyahara MS, Tsuboi H, Yahara M, Yoshimura A, Mayor S, Fujiwara TK *et al* (2010) Membrane molecules mobile even after chemical fixation. *Nat Methods* 7: 865–866

Vega AR, Freeman SA, Grinstein S, Jaqaman K (2018) Multistep track segmentation and motion classification for transient mobility analysis. *Biophys J* 114: 1018–1025

Vershinin M, Carter BC, Razafsky DS, King SJ, Gross SP (2007) Multiple-motor based transport and its regulation by tau. *Proc Natl Acad Sci USA* 104: 87–92

Wegmann S, Eftekharzadeh B, Tepper K, Zoltowska KM, Bennett RE, Dujardin S, Laskowski PR, MacKenzie D, Kamath T, Commins C *et al* (2018) Tau protein liquid-liquid phase separation can initiate tau aggregation. *EMBO J* 37: e98049

Wei M, Fan X, Ding M, Li R, Shao S, Hou Y, Meng S, Tang F, Li C, Sun Y (2020) Nuclear Actin regulates inducible transcription by enhancing RNA polymerase II clustering. *Sci Adv* 6: eaay6515

Xu Z, Schaedel L, Portran D, Aguilar A, Gaillard J, Marinkovich MP, Théry M, Nachury MV (2017) Microtubules acquire resistance from mechanical breakage through intralumenal acetylation. *Science* 356: 328–332

Zhang M, Chang H, Zhang Y, Yu J, Wu L, Ji W, Chen J, Liu B, Lu J, Liu Y *et al* (2012) Rational design of true monomeric and bright photoactivatable fluorescent proteins. *Nat Methods* 9: 727–729

Zhou Y, Hancock JF (2015) Ras nanoclusters: versatile lipid-based signaling platforms. *Biochim Biophys Acta* 1853: 841–849